Low-Resistance Laser-Induced Graphitic Carbon by Maximizing Energy Delivery and Pulse Overlap

*Aamir Minhas-Khan, Suresh Nambi, Gerd Grau**

Department of Electrical Engineering and Computer Science, Lassonde School of Engineering, York University, 4700 Keele Street, Toronto, ON, M3J 1P3, Canada

Abstract

Laser-induced graphitic carbon (LIGC) is a promising technology to manufacture conductive carbon in a cost-effective manner on a flexible substrate with a scanned laser. One limitation preventing the widespread adoption of LIGC in electronic devices and circuits has been its relatively high sheet resistance. Here, we report the lowest sheet resistance to date for LIGC engraved on flexible polyimide of 6.14±0.11 Ω/□. Several general strategies are identified to minimize sheet resistance. Most importantly, the total laser energy per unit area delivered to the substrate needs to be maximized. This can be achieved by increasing laser power, decreasing laser scan speed and increasing overlap between adjacent pulses. Pulse overlap can be increased by increasing linewidth (raster rather than vector mode) and increasing the dots per cm resolution, i.e., decreasing spacing between pulses, which also improves LIGC uniformity. Further, decreasing scan speed increases the ablation threshold because of increased cooling between pulses enabling more energy to be delivered without the material ablating. These insights were obtained using a combination of electrical measurements, thermal modeling and material characterization. With optimized energy delivery, a domain size (L_a) of about 60 nm was obtained, which highlights the high quality of the obtained LIGC material.

* Corresponding author. Email: grau@eecs.yorku.ca. Phone: +1 416-736-2100 Ext. 70127 (Gerd Grau)

Keywords: laser-induced graphitic carbon; low resistance; laser fluence; flexible electronics; low-cost electronics; micro-supercapacitor

1. Introduction

Carbon nanomaterials have been attracting significant attention in recent years due to their superior optical, electrical, physical, mechanical, chemical, and thermal properties and different types of carbon nanomaterials have been used in a variety of devices as active materials. These devices can be employed in electronic systems on flexible, large-area substrates for applications such as wearable healthcare monitoring, microfluidics, low-cost sensor tags, energy generation and storage, or electrocatalysis [1–5]. However, industrial-scale production of carbon materials for devices is a challenge. First, the carbon material needs to be produced, which typically involves chemicals during synthesis that are harmful to humans and the environment as well as involve multiple steps making the process lengthy [6]. Second, the carbon needs to be deposited onto the desired substrate and patterned into the shape of the electrodes or active material of the desired microdevices. A common patterning method is photolithography and etching, which is costly [7]. Printing offers higher throughput and lower-cost manufacturing but still requires separate manufacturing of the carbon and formulation of the ink [8].

Alternatively, patterned conductive carbon can be fabricated with a one-step process by scanning a laser beam over a polymer sheet and converting the polymer to graphitic carbon. This laser-induced graphitic carbon (LIGC) process is fast, simple once laser parameters are optimized, and can be performed under ambient air conditions. After early reports in 1994 using an ultraviolet (UV) laser [9,10], the process was first demonstrated using a CO_2 infrared laser on commercial polyimide (PI) film in 2014 [11]. Since then, there have been many reports of LIGC [3,4,12] predominantly on PI as well as on other substrates such as polydimethylsiloxane (PDMS) [13],

wood [14–16], polyetherimide (PEI) [17] or lignin [18]. LIGC typically exhibits a porous morphology with large specific surface area. This makes it particularly well suited for electrochemical applications such as supercapacitors [11,16,19–24], batteries [25,26] and chemical or biological sensors [27–30] as well as other devices including mechanical sensing [31–33], actuators [34], photodetectors [35] or heaters [36]. A challenge for these microelectronic devices is the electrical resistance of the graphitic carbon. If the LIGC resistance is too large, excessive voltage will be dropped across the LIGC lowering the efficiency of the device. Even more important for real systems is the resistance of interconnects between different devices within a circuit. Because interconnects are long, narrow lines, the material needs to have a low sheet resistance. So far, LIGC does not have a sufficiently low sheet resistance to be a feasible interconnect material, which means LIGC devices still need to be combined with other interconnect materials that tend to be expensive such as silver. Conversely, low-resistance LIGC interconnects could be integrated easily with LIGC active devices, simply by changing the laser parameters for different locations on the substrate [23]. So far, most LIGC reports have focused on optimizing other LIGC properties such as specific surface area or functionalization for electrochemical devices. Therefore, there is a need to understand and optimize LIGC sheet resistance, which is the goal of this article.

Several articles have reported sheet resistance for LIGC. Table 1 gives an overview. To make results comparable, this overview is limited to reports using a PI substrate and a CO_2 laser, which is the most common combination. The lowest sheet resistance (R_{sh}) that has been obtained to date is 9.3 Ω/□. Most reported values lie around the range of 20-30 Ω/□. Most reports study a subset of the three most important laser parameters: laser power, scan speed and pulse spacing. Table 1 lists the values of these parameters in each report that achieved the minimum sheet

resistance. Laser power is typically varied by pulse width modulation (PWM). In some reports, power is quoted in Watts, in other cases as a percentage of the maximum laser power. In Table 1, these percentages were converted to Watts. The spacing between adjacent laser pulses is typically quoted in terms of pulse density, i.e., pulses per inch (PPI) or dots per inch (DPI), in SI units pulses per cm (PPc) or dots per cm (DPc). Not all reports list all parameter values, especially for DPc, which we will show here to be an important factor. It is evident that there is considerable variation in the laser parameters that were used in different reports, although they are generally of similar order of magnitude. It is therefore very difficult for any researcher or manufacturer new to the field to quickly identify optimal settings without extensive experimentation. One attempt to simplify this is to calculate a fluence factor, i.e., the optical energy delivered to the substrate per unit area. However, most previous reports do not calculate this metric including the reports of the lowest sheet resistances. Another challenge is that different reports use different formulae, some calculating total deposited energy per unit area [23], some calculating energy per unit area for one pulse not considering overlap between adjacent pulses [29]. This is especially challenging when comparing different graphitic carbon patterns consisting of either individual lines (vector mode) or wider lines, rectangles and squares consisting of multiple adjacent rows of laser pulses (raster mode). Therefore, a systematic study is needed that fully maps out the effect of the different laser parameters and compares the different methods to calculate fluence factor in terms of their utility to optimize sheet resistance. This is done here. Experimentally observed sheet resistance trends are explained using simulations of the temperature distribution during the laser process as well as material characterization using scanning electron microscopy (SEM), X-ray diffraction (XRD), transmission electron microscopy (TEM), Raman spectroscopy, and X-ray photoelectron

spectroscopy (XPS). These simulations and measurements reveal spatial variations in material quality due to the pulsed nature of the laser process. It is found that a key strategy for the minimization of sheet resistance is increasing DPc. This leads to an increased and more evenly distributed energy delivery to the substrate. With these insights, it was possible to achieve the lowest sheet resistance reported to date for LIGC on PI of 6.14±0.11 Ω/□.

Table 1. Overview of reported sheet resistance values for CO_2 laser on PI substrate as a function of laser conditions. Where necessary, power was calculated from the quoted laser duty cycle and peak power. Most articles did not report the fluence factor and many did not report DPc, which is signified with a dash. Here, the lowest sheet resistance to date of 6.14±0.1 Ω/□ is reported.

Year	Reference	R_{sh} (Ω/□)	Power (W)	Speed (m/s)	DPc	Fluence factor (J/cm^2)
2014	[4]	15	5.4	0.089	393	-
2015	[26]	50	6.75	1.3	-	-
2017	[32]	24	3	0.092	-	-
2018	[18]	18	6	0.020	196	166
2018	[30]	19.75	7	0.1	39	-
2018	[19]	9.3	8	0.25	-	-
2018	[33]	29.1	4.8	0.01	393	-
2019	[23]	30	25	0.068	393	-
2019	[27]	40	0.85	0.016	-	-
2019	[24]	25.7	4.8	-	393	3.5
2020	[29]	10	3.15	0.064	393	-
2020	This work	6.14±0.11	4.5	0.032	472	664

2. Experimental Methods

2.1. Fabrication Process

Figure 1 shows the fabrication process. A flexible sheet of commercially available PI (Kapton, 125 µm thickness) was used as the substrate. Substrates were irradiated in 2.5 cm long lines (vector mode) and 4 mm by 4 mm square shapes (raster mode) using a 75 W CO_2 laser (Epilog Fusion M2 Laser). Further characteristics of the laser beam are wavelength 10.6 µm, spot size

250 µm and focal length of the lens 10 cm. The power of the laser beam is modulated by pulse width modulation. For a duty cycle of 100%, the laser power is 75 W. Subsequently, the term power is used to describe the percentage power or duty cycle. The maximum scan speed is 1.6 m/s. Pattern files were drawn using CorelDraw. The spacing between laser pulses is varied by using four different DPc resolutions: 59 DPc, 118 DPc, 236 DPc and 472 DPc.

2.2. Sheet Resistance Measurement

Sheet resistance was measured using the four-terminal method to eliminate the confounding factors of contact and probe resistance. For squares, a four-point probe resistivity measurement system was used (Signatone Pro-4 Stand with SP4 Four Point Head and Keithley SMU 2450 Source Meter). For lines, silver paste was used to create current supply and voltage measurement electrodes and measurements were taken with a semiconductor parameter analyzer (Keithley 4200A).

2.3. Calculation of Fluence Factors

In order to better understand the effect of different laser parameters, the fluence factor was calculated for different experimental conditions. Different formulae were used to calculate the energy per unit area for squares and lines, per unit length for lines and per pulse. These different metrics were compared to elucidate which describes the LIGC process most accurately and is most useful for sheet resistance minimization. During the irradiation, i.e., engraving process, the most important parameters that were varied are DPc resolution (N), scan speed (v), percentage power (x) and pattern. The maximum power of 75 W is denoted as P. The spacing between consecutive pulses can be calculated as 1/N. Therefore, the time between two consecutive laser pulses, i.e., pulse period (T) can be obtained by 1/(Nv). Since the laser is turned on for only a fraction of each period, the length of substrate that is irradiated by each pulse can be calculated

as x/N and the temporal pulse width is xT = x/Nv. The energy delivered by each pulse (E_P) can be calculated by multiplying instantaneous power (P) with temporal pulse width. Thus, the energy per pulse scales inversely with DPc resolution N.

$$E_P = \frac{xP}{Nv} \quad (1)$$

While engraving a line of length L, the number of pulses within the line is given by N*L . Therefore, the energy per unit length (E_L) can be obtained as follows:

$$E_L = E_P \times \frac{NL}{L} = \frac{xP}{Nv} \times N = \frac{xP}{v} \quad (2)$$

Figure 1 (b) (i) illustrates the spacing of pulses within a line for different DPc values. Notably, the energy per unit length in a single line is independent of the DPc resolution N.

The energy per unit area in a line (E_{AL}) can be calculated by diving E_L by the width of the irradiated area, which is the width of the laser beam (w). If a line consists of multiple rows of pulses (see Figure 1 (b) (ii)), the total energy needs to be multiplied by the number of passes (n). In this case, the width of the line is increased by the spacing between passes (1/N) multiplied by the number of passes less one. Thus, E_{AL} is a weak function of DPc when the number of passes is more than one:

$$E_{AL} = \frac{xPn}{v} / \left(w + \frac{n-1}{N}\right) \quad (3)$$

Similarly, energy delivered per unit area (E_{AS}) while engraving a square pattern of area L*L with resolution N can be obtained as follows:

$$E_{AS} = E_P \times \frac{NL \times NL}{L \times L} = \frac{xP}{Nv} \times N^2 = \frac{xP}{v} N \quad (4)$$

Due to the increased overlap between pulses for larger DPc (see Figure 1 (b) (iii)), the energy per unit area in squares scales with N.

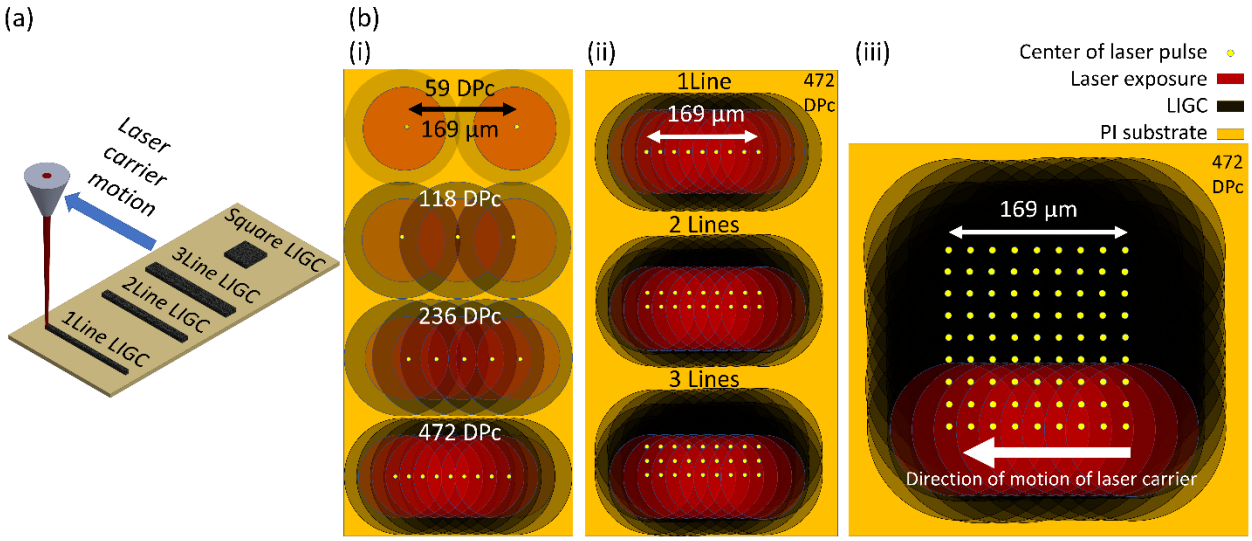

Figure 1. Illustration of (a) LIGC formation process on the surface of the PI sheet using a pulsed CO_2 laser; (b) (i) single line engraving at 59 DPc, 118 DPc, 236 DPc and 472 DPc resolution; (ii) 1, 2 and 3 pulses wide line engraving at 472 DPc; and (iii) square engraving at 472 DPc. Note how the overlap between pulses increases with increasing DPc and from individual lines to multiple lines and ultimately squares i.e. transitioning from vector to raster mode.

2.4. Thermal Modeling

The thermal processes during laser irradiation were simulated to gain further insights into the spatial and temporal temperature distribution not readily accessible experimentally. A time-dependent 3D COMSOL Multiphysics model was created based on the model reported by Ruan et al [39]. Details of the model can be found in the supplementary information. In short, the model simulates the optical absorption of the laser beam on the PI substrate and solves the heat diffusion equation. The laser beam is modeled as a Gaussian beam profile and absorption is modelled using the Beer-Lambert law. Radiative cooling is included for the top surface of the material. Material properties are temperature dependent. Temperature-dependent thermal

conductivity [40] and specific heat capacity [41] of PI were taken from literature. The material is assumed to degrade at the pyrolysis/ carbonization temperature T_d = 858 K as determined by thermogravimetric analysis (TGA) [39,42] and behaves as carbonaceous material with large absorption coefficient thereafter [39]. This temperature is reached very fast compared to the pulse on-time due to the high optical power density in our process. Therefore, optical behavior is dominated by the behavior of carbonaceous material. Ruan et al implemented the model for a single laser pulse creating a circular graphitic carbon spot on PI. Here, the model is extended to study lines that are made up of multiple overlapping laser pulses (see Figure 1 for an illustration of the scanned laser process). The laser is modelled as a moving heat source, which is periodically turned on for a specific time each pulse. The effect of the same laser parameters that were studied experimentally were studied by simulation: DPc, duty cycle (percentage power) and scan speed. The graphitic carbon linewidth was determined from simulated temperature profiles by treating all positions that had reached at least a temperature of T_d as LIGC.

2.5. Material Characterization

A field emission scanning electron microscope (FE-SEM) (Thermofisher Quanta 3D) was used to observe the morphology of the LIGC. XRD was conducted on a Philips powder XRD system (PW1830 generator, PW3710 goniometer) with Cu K-alpha radiation (wavelength 1.54 Å). Match software was used for curve fitting. Each wide-range XRD scan was conducted using 2θ values between 15° and 60° with 2θ step values of 0.02° taken in 2.5 seconds, and each single XRD peak was scanned at a lower scan rate with 2θ step values of 0.01° in 10 seconds. Crystallite sizes L_a and L_c were calculated from XRD results using the Scherrer equation [43]:

$$L_a = \frac{1.84\lambda}{B_{1/2}(2\theta)\cos(\theta)} \quad (5)$$

$$L_c = \frac{0.89\lambda}{B_{1/2}(2\theta)\cos(\theta)} \quad (6)$$

Where λ is the X-ray wavelength (1.54 Å), θ is the Bragg angle of the peak, $B_{1/2}(2\theta)$ is the full width at half maximum (FWHM) of the peak at angle 2θ fitted with Gaussian curve fitting. TEM images were obtained on a Talos L120C TEM (Thermo Scientific) using a LaB_6 filament operating at 120 kV. Images of the LIGC were acquired with a Ceta 4k x 4k CMOS camera. Raman spectra were obtained with a Bruker Senterra Dispersive Raman Microscope using a 532 nm wavelength laser with 1.5 µm spot diameter and laser excitation power of 10 mW. Crystallite size was calculated using equation (7):

$$L_a = (2.4 \times 10^{-10}) \times \lambda_l^4 \times \left(\frac{I_G}{I_D}\right) \quad (7)$$

Where λ_l is the wavelength (532 nm) of the laser source for the Raman measurements. I_G and I_D are the integrated peak intensities respectively of the G- and D-peak fitted with a Voigt function. XPS was performed using Al Kα X-ray radiation using a Thermo Scientific K-Alpha XPS spectrometer. The survey spectra were recorded with 1 eV step size and elemental spectra were recorded with 0.02 eV step size. Peak fitting of the XPS data was carried out using XPSPEAK41 software.

2.6. Micro-Supercapacitor Fabrication and Characterization

To demonstrate a micro-supercapacitor application, we prepared two interdigitated in-plane electrodes of LIGC with 0.032 m/s laser scan speed, 7% laser power, 1.3 mm width of each electrode and 0.7 mm spacing between them. Silver paste was applied on both electrodes and it was separated from the interdigitated active area by PI taping. A gel electrolyte was drop cast over the shared interdigitated area, the device was exposed to vacuum for 2 hours, and placed in ambient conditions for one day before electrochemical testing. The electrolyte was prepared by

stirring 10 ml of deionized water, 1 ml of H_2SO_4 and 1 g of polyvinyl alcohol (PVA) for 1 hour at 80 °C.

The devices were characterized electrochemically by cyclic voltammetry (CV) and constant current charge-discharge measurements using a Metrohm PGSTAT204 potentiostat/galvanostat. Based on CV curves, specific areal capacitance C_A is calculated using equation (8):

$$C_A = \frac{1}{2 \times S \times \nu \times (V_f - V_i)} \int_{V_i}^{V_f} I(V) dV \quad (8)$$

where S is total active electrode area of a device, ν is voltage sweep rate, I(V) is voltammetric current, and V_f and V_i are the initial and final potentials, 0 V and 1 V, respectively, of the CV curves.

Specific areal capacitance from galvanostatic discharging curves was calculated using equation (9):

$$C_A = \frac{2i}{S \times \left(V^2 \Big|_{V_i}^{V_f}\right)} \int_{t_i}^{t_f} V(t) dt \quad (9)$$

Where i is discharging current, S is total active electrode area, V_f and V_i are final and initial values of potential V, and similarly t_f and t_i are final and initial values of time t.

Specific energy E_A and power P_A densities were calculated by using equations (10) and (11), respectively:

$$E_A = \frac{1}{2} \times C_A \times \frac{(\Delta V)^2}{3600} \quad (10)$$

$$P_A = \frac{E_A}{\Delta t} \times 3600 \quad (11)$$

Where ΔV is potential difference between final and initial potentials $V_f - V_i$ during discharging and Δt is discharge time.

3. Results and Discussion

3.1. Sheet Resistance

Here, we report the lowest sheet resistance to date for LIGC on PI substrate of 6.14±0.11 Ω/□. In order to achieve this sheet resistance, a deep understanding of the interaction between laser scan speed, power, DPc and pattern is required. There exists a window of conditions under which LIGC can be formed. Figure 2 (a) shows this window as a function of laser scan speed and power for squares at 472 DPc (see Figure S1 for optical images of the samples). No graphitic carbon can be produced for power below a particular value called threshold power, and all powers higher than a particular value called ablation power ablate the material. Furthermore, this window of workable power from threshold to ablation shifts towards higher power values as the speed of the carrier increases. Under ambient air conditions, preventing ablation is a critical problem to achieve high-quality LIGC [16,17].

Within this process window, the sheet resistance of the graphitic carbon varies by several orders of magnitude. Measured sheet resistance values for squares are shown in Figure 2 (b)-(c). The trend of sheet resistance with energy per pulse (Figure 2 (b)) is not very clear. For each value of DPc individually, sheet resistance decreases as pulse energy increases. However, between different DPc values, sheet resistance is lowest for the highest DPc (472), which has the lowest pulse energy within the workable window. Thus, energy per pulse is not a good parameter to understand the LIGC process in squares. Conversely, energy per unit area (Figure 2 (c)) is a much better predictor of sheet resistance. Sheet resistance decreases mostly monotonically with increasing energy per unit area across different values of DPc. This means that to achieve the

lowest sheet resistance, one needs to increase the optical input energy per unit area as much as possible. With high DPc, closely spaced laser pulses can deliver a large amount of energy per unit area as it scales linearly with DPc (see equation (4) and Figure 1 (b)) even though each individual pulse is low in energy.

However, the limit to the energy per unit area that can be achieved is the ablation threshold. Plotting the energy per unit area at the ablation threshold (see Figure 2 (d)) vs speed for different DPc reveals two important insights. Firstly, ablation threshold energy per unit area decreases with increasing laser carrier speed. This is the reason why the lowest sheet resistance is observed at low speed. To explain this, the dynamics of the heating process need to be considered, which is done using a thermal finite element model (see section 3.2). Secondly, increased DPc leads to an increased ablation threshold energy per unit area. This is again due to the fact that energy per unit area scales linearly with DPc. One can also consider the ablation threshold energy per unit length of line within each row of the square, which is the same as power divided by speed (see Figure 2 (e)). Again, the threshold energy falls with increasing laser scan speed. However, all curves for different DPc fall on top of each other. This means that for ablation the most important parameter is energy per unit length at a given speed, not energy per unit area or energy per pulse (see Figure S2). Energy per unit length determines the peak temperature that is reached within a single laser pass causing ablation if the temperature is too high. Since squares here are relatively large (4 mm side length), the material has time to cool down between passes, i.e., rows. Therefore, the total energy per unit area does not affect peak temperature and ablation significantly. However, total energy per unit area after multiple passes determines sheet resistance because the material is further converted on each pass.

(a)

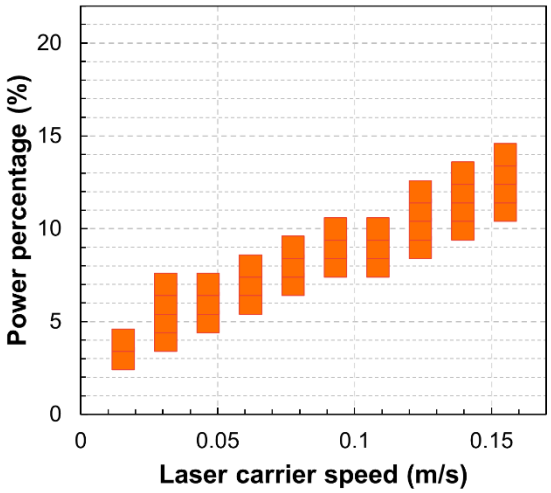
Power percentage (%)
0
5
10
15
20
0
0.05
0.1
0.15
Laser carrier speed (m/s)

(b)

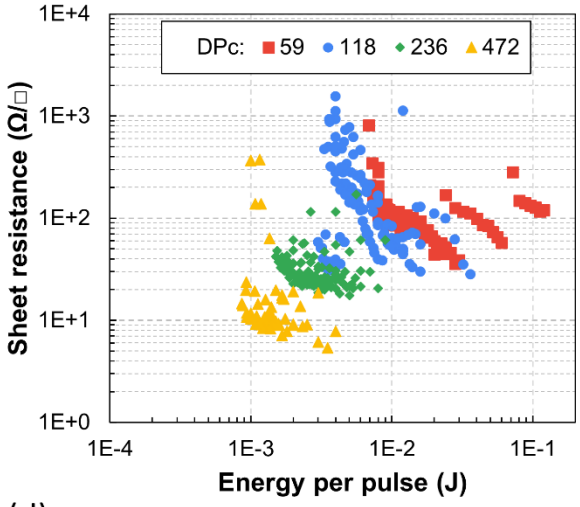
DPc: 59 118 236 472
Sheet resistance (Ω/□)
1E+0
1E+1
1E+2
1E+3
1E+4
1E-4
1E-3
1E-2
1E-1
Energy per pulse (J)

(c)

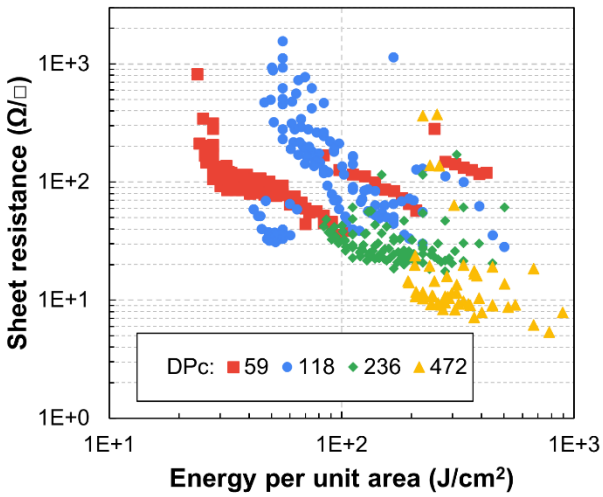
Sheet resistance (Ω/□)
1E+0
1E+1
1E+2
1E+3
DPc: 59 118 236 472
1E+1
1E+2
1E+3
Energy per unit area (J/cm²)

(d)

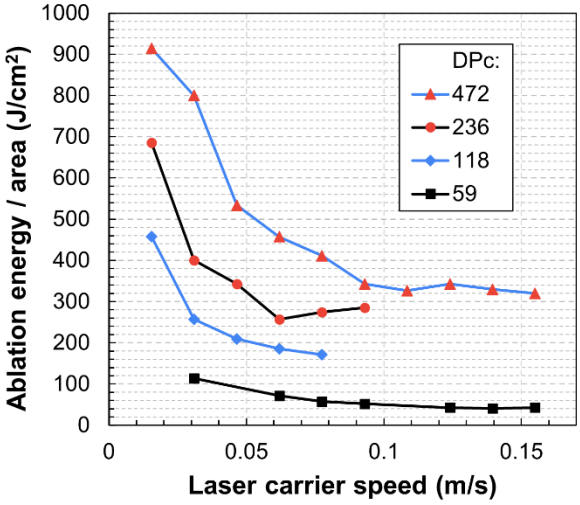
Ablation energy / area (J/cm²)
0
100
200
300
400
500
600
700
800
900
1000
DPc:
472
236
118
59
0
0.05
0.1
0.15
Laser carrier speed (m/s)

(e)

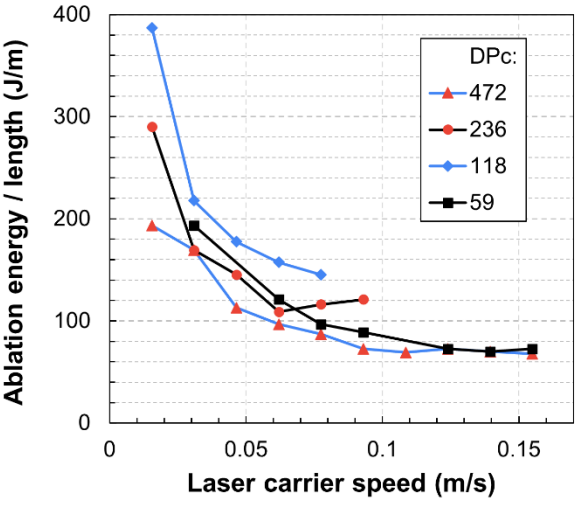
Ablation energy / length (J/m)
0
100
200
300
400
DPc:
472
236
118
59
0
0.05
0.1
0.15
Laser carrier speed (m/s)

274

Figure 2. Electrical results for squares. (a) Power window for conductive LIGC generation as a function of laser scan speed for 472 DPc. (b) Sheet resistance decreases with pulse energy for each DPc value but not when comparing different DPc. (c) Sheet resistance decreases with energy per unit area across different DPc values. (d) The highest energy per unit area that can be reached is limited by the ablation threshold and is largest for 472 DPc at low speed. (e) Ablation threshold energy per unit length also decreases with increasing laser scan speed. It does not vary significantly with DPc meaning that, for a given speed, ablation threshold power can be predicted by calculating energy per unit length.

To further distinguish the differences between lines and squares, the sheet resistance of individual lines was studied. Lines were 1, 2 or 3 pulses wide with spacing between passes determined by DPc. The laser scan speed that gives the lowest sheet resistance for squares was further studied for lines (0.032 m/s). Lines exhibit the same trends as squares. Again, pulse energy is not a good predictor of sheet resistance because it exhibits opposite trends for constant DPc and between different values of DPc (see Figure 3 (a)). Energy per unit area can predict sheet resistance better with generally lower sheet resistance for larger energy per unit area (see Figure 3 (b)). However, there are some secondary trends that cannot be explained with this simple model based on just an analytical energy calculation. Sheet resistance again decreases with increasing DPc. But the effect is much weaker than for squares where it is mainly due to the larger energy per unit area for larger DPc. Conversely, in lines, the energy per unit area only weakly depends on DPc and not at all for lines of width one pulse. This effect can be explained by the increased overlap between pulses for larger DPc. This is especially pronounced for DPc = 59 where pulses barely overlap, and sheet resistance is high. Also, sheet resistance decreases

with increasing line width even for the same energy per unit area. Lines that are three pulses wide exhibit a similarly low sheet resistance as squares with the same energy per unit area. Again, this can be explained by the overlap between subsequent laser passes exposing the material multiple times. To further understand these secondary effects, finite element modeling of the thermal process in a single line was performed.

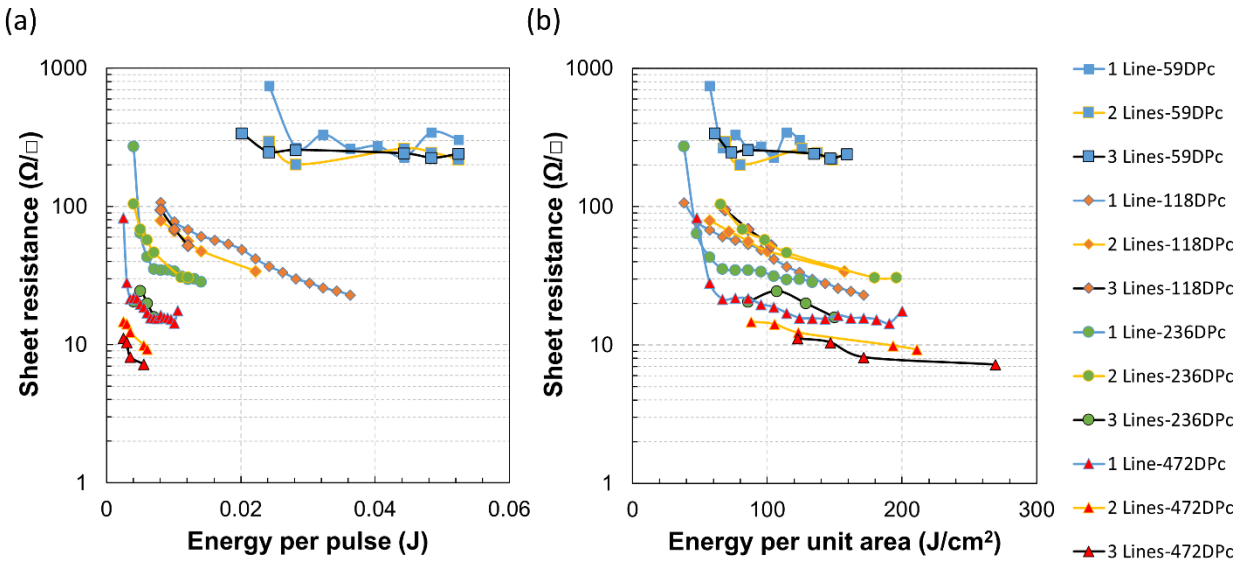

Figure 3. Electrical results for lines that are 1, 2 or 3 pulses wide at 0.032 m/s. (a) Sheet resistance decreases with pulse energy for each DPc value but not when comparing different DPc. (b) Sheet resistance decreases with increasing energy per unit area. Sheet resistance also decreases with increasing DPc and increasing linewidth.

3.2. Thermal Model

The above calculations of fluence factor give a useful single parameter for process optimization. However, this simplicity limits its usefulness to understand the underlying processes. To gain more understanding, the temperature distribution during the LIGC process was simulated for a line. Figure 4 (a) shows an example of the simulated temperature profile of a line. The PI substrate has been cut along the symmetry plane (i.e., along the length of the line in the y-

direction and the z-direction into the substrate) to reveal the cross-sectional temperature profile in addition to the temperature profile of the top surface. The image is taken just after the 16^{th} pulse out of 32 pulses that make up this simulated LIGC line. One can observe a strong hot zone corresponding to where the laser pulse last irradiated the substrate. Additionally, one can observe a temperature gradient in the x- and z-direction due to heat diffusion. The laser is scanned in the positive y-direction. One can observe elevated temperatures behind the current pulse where previous pulses have irradiated the surface and the material has not fully cooled down yet.

To validate the model, the experimental linewidth was compared with linewidth obtained from simulation. Experimental linewidth was obtained from optical microscopy where the LIGC can be clearly observed as black material (see Figure S3). The smallest experimental linewidth is 275 µm, which is limited by the spot size of the laser of 250 µm. Linewidth from simulation was determined following the assumption of Ruan's model that LIGC is formed when the temperature at any point exceeds T_d = 858 K [39]. Figure 4 (b) shows that both experimental and simulated linewidth agree well and follow the same trend of increasing linewidth with increasing percentage laser power. The average error is 9.5%. This demonstrates that the model accurately captures trends in the LIGC process for lines despite of the model's simplifying assumptions.

Experimentally, it was observed that lower scan speed results in the lowest sheet resistance due to an increased threshold ablation energy. In order to understand this effect further, simulations were performed for lines with different laser scan speeds. The power percentage was scaled with speed to keep the total optical energy transferred to the substrate constant. Energy is proportional to power divided by speed. Figure 4 (c) shows the temperature evolution with time at the center point of a 32-pulse line for one case with speed 0.032 m/s and one case with speed 0.16 m/s. DPc was 472 in both cases. One can clearly observe how individual pulses heat the center point

successively. At first, heating is gradual as only the outer part of the Gaussian beam profile hits the center point of the line. When the center of the laser is right at the center of the line, temperature reaches its maximum value. For the slower scan speed, the maximum temperature is about 6,600 K whereas the faster scan speed reaches about 8,400 K. This occurs despite of the fact that the on-time and energy deposited by each pulse are the same. The reason for this difference is the different time available for cooling between pulses. In the 0.16 m/s high-speed case, there is insufficient time for cooling in between pulses. The temperature does not drop below the sublimation temperature of graphite of 4,000 K for most of the simulation time. Therefore, it can be expected that the material will be substantially ablated, which agrees with our experimental results for this condition. It should be noted that the simulation does not model the vaporization of material, which is a complex process. Therefore, large peak temperatures should not be understood as the solid material actually reaching this temperature, but rather as portions of the material vaporizing. The power of the simulation lies not in the quantitative prediction of temperature values, especially for very high peak temperatures; rather, it enables the comparison between different laser conditions and the explanation of experimental trends. Conversely, the slower speed of 0.032 m/s gives more time for cooling resulting in a lower minimum temperature of about 2,000 K right before each pulse and subsequently a lower peak temperature after each pulse. The same deposited laser energy is spread out over a longer period of time leading to a lower overall temperature profile. This promotes the formation of high-quality graphitic carbon without the rapid temperature rise observed at high speed that causes ablation. The peak temperature is still very high, but only for a few microseconds and in a thin layer on the surface of the material. One would therefore expect a limited amount of material vaporization, which corresponds well to the fact that these conditions are close to the threshold

for full ablation and the porous microstructure of the resulting LIGC film (see SEM results in section 3.3). In practice, this creates a trade-off between decreasing sheet resistance and increasing laser scan speed for high manufacturing throughput.

DPc is an important parameter that determines how temperature is distributed spatially during the LIGC process. Experimentally, it was found that larger DPc leads to lower sheet resistance. In squares, this can be explained with the fact that energy per unit area is largest for large DPc. In single lines, energy per unit area does not depend on DPc but sheet resistance still does, although not as strongly as in squares. To explain this, the spatial temperature profile along a line was simulated for DPc of 118, 236 and 472. Figure 4 (d) shows the maximum temperature during the simulation for every point along the center axis of the line (y-axis). One can observe that the peak temperature increases with decreasing DPc. It is about 6,900 K for 472 DPc, 8,400 K for 236 DPc and 10,000 K for 118 DPc. Temperature uniformity increases with increasing DPc. This occurs because each pulse has less energy for higher DPc, but the number of pulses is larger. All three lines have the same length, but for 472 DPc the line consists of 32 pulses, for 236 DPc of 16 pulses and for 118 DPc of 8 pulses. Gaussian pulses are more closely spaced and overlap more for larger DPc. It is advantageous to achieve a uniform temperature distribution rather than high peak temperatures, which causes vaporization. This applies both in terms of temporal temperature distribution (controlled by laser scan speed) and in terms of spatial temperature distribution (controlled by DPc). However, there again exists a trade-off between graphitic carbon quality and manufacturing throughput. When DPc is increased for squares, the same square pattern will consist of more rows that require more laser passes.

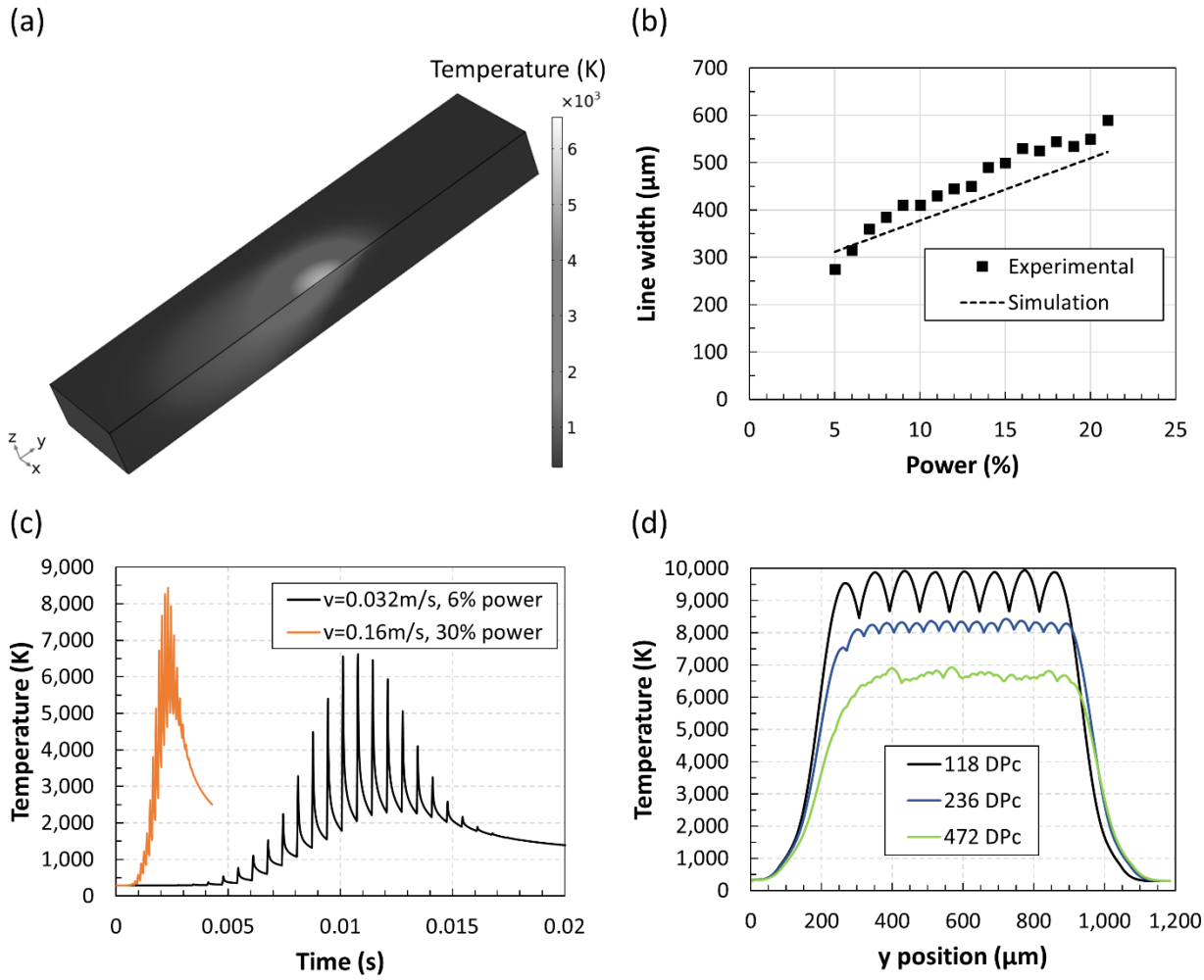

Figure 4. (a) Simulated temperature profile after 16 pulses for 472 DPc, 6% power and 0.032 m/s. The laser is scanned in the y-direction. PI substrate is cut along the y-z symmetry plane for visualization of the depth profile. (b) Comparison between experimental and simulated LIGC linewidth vs power validating the model (472 DPc, 0.032 m/s). (c) Temperature at the center of a 32-pulse line for 472 DPc for two different scan speeds. Power was scaled with speed to keep delivered energy constant. The faster scan speed reaches a higher peak temperature due to the decreased time for cooling between subsequent pulses. (d) Maximum temperature recorded during the simulation as a function of position along the center axis of the LIGC line on the top surface of the substrate (6% power, 0.032 m/s). Peak temperature decreases with increasing DPc and uniformity also improves with increasing DPc as Gaussian pulses have less energy and overlap more.

3.3. Material Characterization

To further understand the LIGC process and confirm some of the insights gained from resistance measurements and thermal simulation, the resulting graphitic carbon material was characterized by SEM, XRD, TEM, Raman spectroscopy, and XPS. We focused on the condition that resulted in the best sheet resistance (squares with 472 DPc, speed 0.032 m/s) and investigated different values of power.

Figure 5 (a-d) shows SEM top-view images fabricated at 4%, 5%, 6% and 7% power. This covers the workable power range for LIGC generation in squares at 0.032 m/s and 472 DPc. Graphitic carbon flakes can be made out more clearly as power increases. At 4% power, flakes are not very clear. At 7% power, one can clearly observe graphitic carbon flakes emerging from the substrate. This agrees with electrical results. Sheet resistance decreases as power is increased from 4% to 7%. Since speed and DPc are held constant, the deposited energy also increases directly with power, which results in better material quality. In between graphitic carbon flakes, there exist pores. LIGC at 4% power exhibits only a small number of small pores. Pore density and size increases with power and the most prominent pores are found for 7% power. LIGC generated with 7% power conducts but also exhibits partial ablation (see Figure S1). There exists significant disorder but pore size and spacing corresponds approximately to the laser pulse spacing of 21 μm at 472 DPc.

LIGC engraved at 5%, 6% and 7% power was further characterized using XRD. The results exhibit two peaks at 2θ angle values of 26.1° and 42.7° (see Figure S4 for full scan and Figure 5 (e) for high-resolution scans of peaks) due to diffraction from the (002) and (100) planes, respectively. The interlayer spacing of the (002) plane, calculated using Bragg's diffraction law from the corresponding 2θ angle value of 26.1°, is 3.41 Å, which is close to the expected value

for graphite. Crystallite size calculated from the Scherrer equation is shown in Table 2 and discussed in the context of L_a values obtained from Raman spectroscopy. Figure 5 (f) shows high-resolution transmission electron microscopy (HRTEM) of the LIGC engraved at 7% laser power. The spacing between ten layers is measured as 3.4 nm, i.e., the lattice spacing is 3.4 Å, which is consistent with the XRD data.

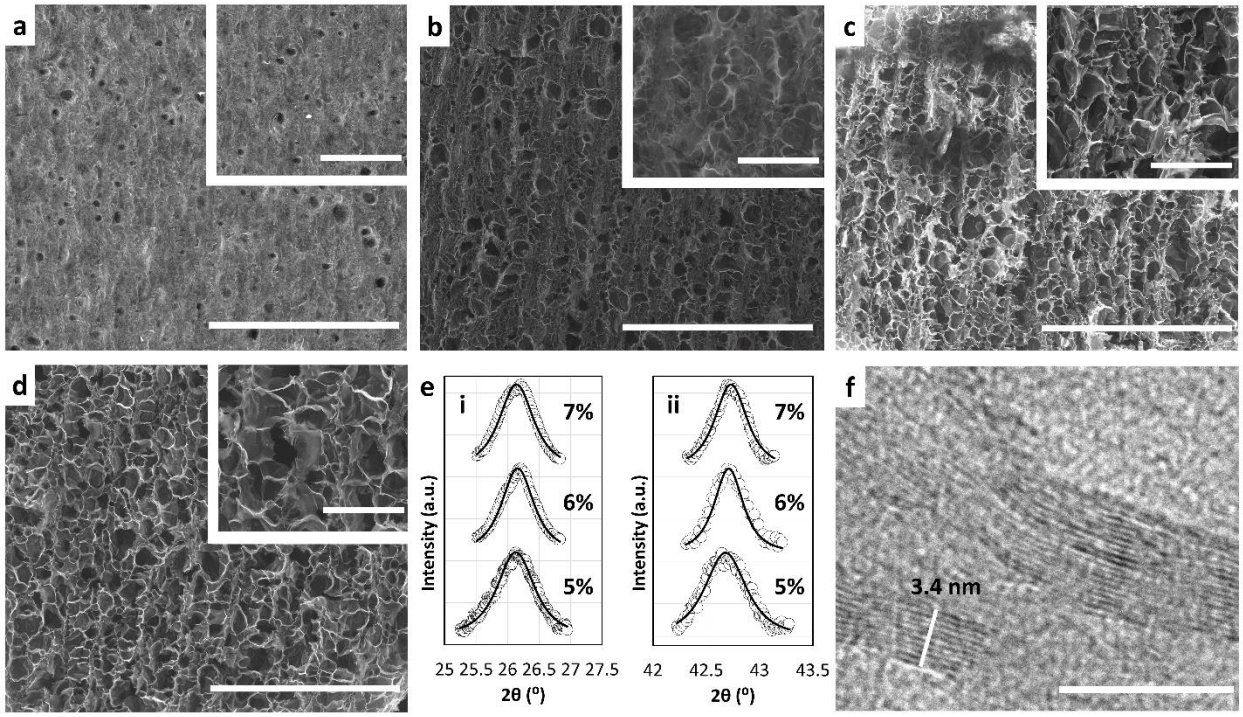

Figure 5. SEM images for LIGC squares fabricated at 472 DPc and 0.032 m/s speed with (a) 4%, (b) 5%, (c) 6%, and (d) 7% power (scale bar: 200 μm). Insets are higher magnification SEM images (scale bar: 40 μm). (e) XRD peaks of material engraved at 5%, 6% and 7% power (i) (002) peak and (ii) (100) peak. (f) HRTEM image of LIGC engraved at 7% laser power (scale bar: 10 nm).

Raman spectroscopy is a sensitive and non-destructive technique for molecular level characterization of carbon-based materials. It is a powerful technique to monitor the structural

changes of graphitized material. Figure 6 (a) shows representative Raman spectra for squares with power ranging from 4% to 8% at 472 DPc and 0.032 m/s. They show three prominent peaks typical for graphitic carbon: the D, G, and 2D bands at Raman-shift values around 1350 cm^{-1}, 1580 cm^{-1}, and 2700 cm^{-1}, respectively [11,44]. The G band is the most important peak for graphene or graphite, also named graphitic peak. The 2D band appears because of the 2^{nd} order zone-boundary phonons [45]. All samples with measurable conductivity exhibit the 2D peak; however, 8% power does not conduct and also does not exhibit a 2D peak as material is ablated. For the other LIGC samples studied here, the peak ratio between the G and the 2D peak (I_G/I_{2D}) increases with power getting closer to 2 (1.43 for 6% power). A single 2D peak is observed with a FWHM of 47.5 cm^{-1} for 6% power. This is characteristic for turbostratic graphite, which lacks AB stacking, in contrast to crystalline graphite that exhibits multiple 2D peaks and single-layer graphene whose FWHM is smaller [45–48]. The D band appears because of edges, defects or bent sp^2 carbon bonds in the material, which disappears in pure graphite and infinite graphene sheets [49]. Therefore, a high-quality crystal of graphite exhibits a high G to D band ratio (i.e., I_G/I_D, where I_G and I_D are the integrated values over the G and D bands, respectively). Figure 6 (b) shows the average I_G/I_D ratio as well as the sheet resistance for LIGC squares from 4% to 8% power. As power increases, material quality improves, which manifests itself as increased I_G/I_D ratio and decreased sheet resistance. The highest I_G/I_D ratio of 3.1 is observed at 6% power. At 7% power, sheet resistance is slightly lower than at 6% power (5.36±0.12 Ω/□ vs 6.14±0.11 Ω/□); however, the LIGC partially ablates, which is evident optically as well as in the decreased I_G/I_D ratio. At 8% power, ablation is more substantial, sheet resistance cannot be measured anymore and I_G/I_D drops further.

453 The crystallite size L_a was calculated from these Raman results in terms of I_G/I_D ratio using
454 equation (7) and compared with L_a and L_c results from XRD using the Scherrer equations (5) and
455 (6). All L_a and L_c values calculated from XRD and Raman results are shown in Table 2. The
456 samples' crystallite sizes calculated from the two different measurements are in good agreement.
457 Again, 6% power gives the largest crystallite size of about 60 nm for L_a (54.5 nm by XRD and
458 60.3 nm by Raman). Both L_a and L_c increase with increasing power from 5% to 6%. At 7% and
459 8% power, crystallite size decreases as material starts to be ablated. Many other researchers have
460 also reported these improvements in crystal quality, domain size, and electrical performance with
461 increasing laser power [11,18,50–54]. However, such large domain sizes have not been reported
462 before, which is an explanation for the low electrical resistance reported here.

463 Table 2. Comparison of the crystallite size from XRD and Raman for different laser powers (472
464 DPc, 0.032 m/s). Note, material at high laser power of 8% was ablated, Raman was performed
465 for a very small trace of the ablated material, but the material quantity was insufficient for XRD.

Sample Power (%)	Crystallite size		
	XRD		Raman
	L_c (nm)	L_a (nm)	L_a (nm)
5	11.5	37.9	39.3
6	13.4	54.5	60.3
7	12.6	48.4	47.2
8	N/A	N/A	36.9

466

467 However, considering a single average I_G/I_D number for each sample only partially captures the
468 quality of theLIGC. It varies for different positions across each sample. Figure 6 (c) shows the
469 I_G/I_D ratio at different positions within a square generated with 4% power. Corresponding
470 position-dependent Raman spectra are shown in Figure S5 as well as Figure S6-S9 for 5-8%

laser power samples. The Raman measurement was scanned horizontally and vertically crossing multiple laser pulses. One can note that the I_G/I_D ratio, i.e., the graphitic carbon quality, varies periodically with position. The periodicity corresponds to the spacing between laser pulses, i.e., the inverse of DPc, which is 21 µm for 472 DPc. Pulses are spaced equally in the x-direction along the laser scan direction and the y-direction orthogonal to the scan direction. Therefore, the periodicity is the same in both directions. A similar result is obtained when creating a 2D map of I_G/I_D ratio (see Figure 6 (d) for 6% power). Within this area, whose size corresponds to the spacing between pulses in x and y, only one maximum in I_G/I_D ratio is observed again confirming that graphitic carbon quality varies periodically with pulse spacing. This occurs because adjacent pulses do not overlap perfectly due to the Gaussian beam profile with intensity variations between pulses. This leads to the variations in graphitic carbon quality corresponding to the pulse spacing.

In order to study the effect of pulse overlapping further, Raman spectra were measured along the length of individual lines for different DPc values (see Figure 6 (e) and Figure S10). The power (6%) and speed (0.032 m/s) values correspond to the highest-quality squares with 472 DPc. The I_G/I_D ratios obtained are markedly lower than for squares. This agrees well with sheet resistance, which is also higher for individual lines than squares at the same power and speed. For squares, pulses overlap in two dimensions: aligned with the laser scan direction and orthogonal with multiple rows overlapping. This means that more energy per unit area is delivered to the substrate by subsequent overlapping pulses for squares. For single lines, energy per unit area is independent of DPc. As DPc increases, each pulse is less energetic, but this is compensated for by the increased pulse density. Therefore, sheet resistance and I_G/I_D ratio are weaker functions of DPc for lines than for squares. However, even for lines, there is still a positive correlation

between increasing DPc and decreasing sheet resistance. This may be explained by the more uniform material generated with larger DPc. Figure 6 (e) shows that the I_G/I_D ratio varies periodically along the length of LIGC lines. The periodicity again corresponds to the pulse spacing (84 µm for 118 DPc, 42 µm for 236 DPc, 21 µm for 472 DPc). 472 DPc exhibits the smallest variations. This means there are no regions with low material quality that increase the total resistance of the line. The variations in I_G/I_D ratio along the line correspond to variations in peak temperature during the laser process found by simulation (cf. Figure 4 (d)). For lower DPc, one can clearly observe the peak of the Gaussian profile of each laser pulse in the simulated temperature profile. For higher DPc, pulses are less energetic and spaced closer together repeatedly heating the substrate. This results in both a more uniform temperature profile and more uniform material quality.

Therefore, to achieve low sheet resistance and good overall material quality, it is important to maximize overlap between laser pulses by increasing DPc and designing patterns consisting of multiple closely spaced rows of pulses (raster rather than vector mode). Lines that are three pulses wide already approach the sheet resistance of squares that are effectively infinitely wide. Sheet resistance is improved primarily because more total optical energy per unit area is delivered to the substrate and secondarily because more pulse overlap results in more uniform material. In the future, these insights could be combined with other strategies to increase overall energy delivery such as defocusing or multiple lasing [17] to potentially further reduce sheet resistance. Further increases in DPc could also lead to further reduced sheet resistance. Finally, it should be noted that the periodic variations in material quality should be considered when characterizing LIGC using Raman spectroscopy in the future by scanning over an area corresponding to the periodicity of the laser pulses.

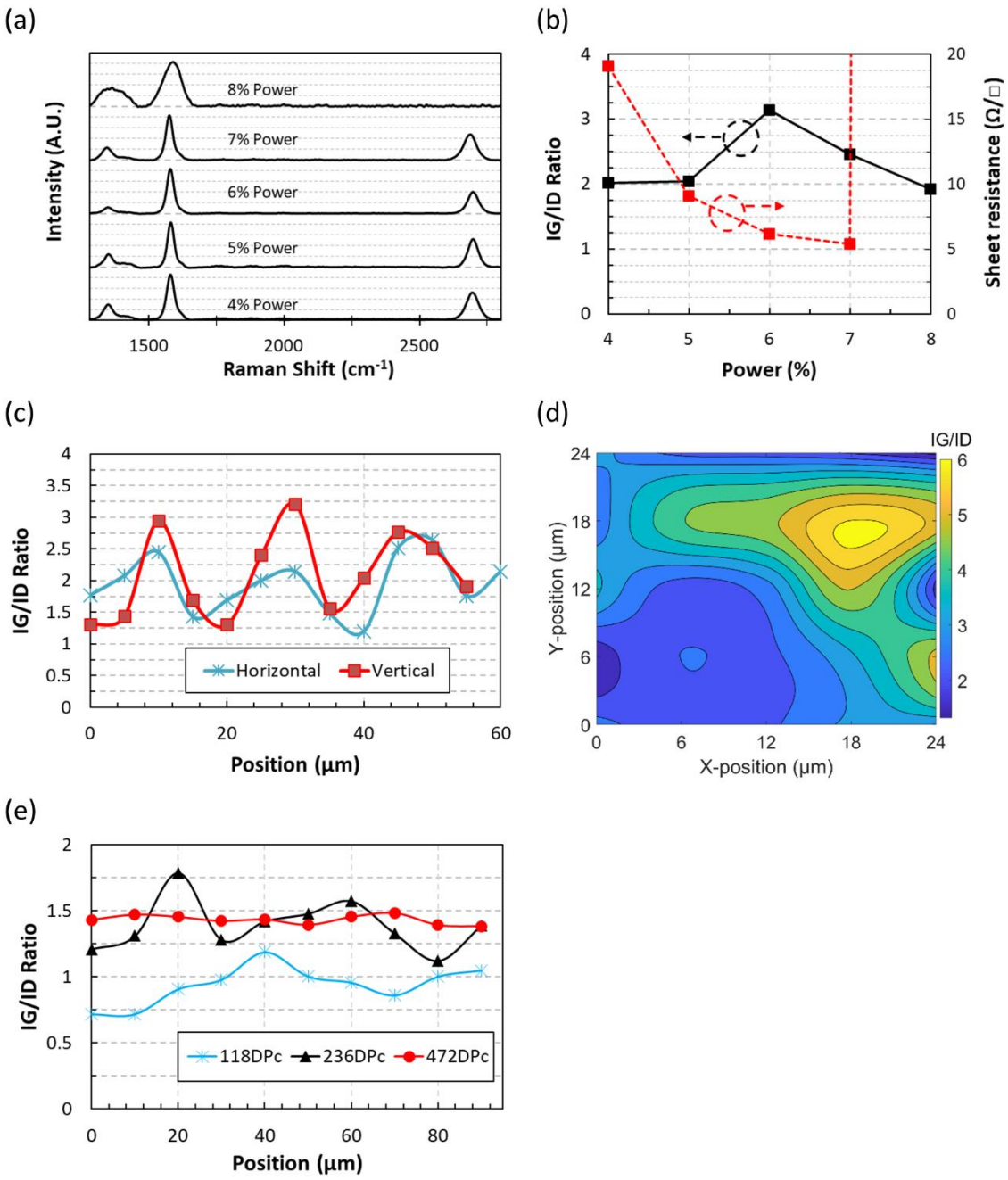

Figure 6. (a) Raman spectra for LIGC squares at 472 DPc and 0.032 m/s spanning the workable power range. Spectra exhibit the typical graphene peaks (G, 2D and D) except for 8%, where material ablates. Material partially ablates for 7% power. (b) Average I_G/I_D ratio extracted from Raman spectra and sheet resistance against laser power. I_G/I_D ratio increases and sheet resistance decreases with increasing power up to 6% power beyond which material quality deteriorates. (c) I_G/I_D ratio at different positions within LIGC square (4% power, 472 DPc, 0.032 m/s). Periodic variations correspond to laser pulse spacing of 21 μm. Horizontal scan=aligned with laser scan

direction, vertical scan=perpendicular to laser scan direction. (d) I_G/I_D ratio at different positions within LIGC square (6% power, 472 DPc, 0.032 m/s). Only one maximum is observed within this 2D map of size corresponding to pulse spacing. (e) I_G/I_D ratio at different positions along LIGC lines with different DPc (6% power, 0.032 m/s, one pulse wide). I_G/I_D ratio varies periodically with position corresponding to pulse spacing. With increasing DPc, minimum I_G/I_D ratio increases and non-uniformity decreases.

Furthermore, XPS survey spectra of LIGC fabricated at 5%, 6% and 7% laser power with all other conditions constant are shown in Figure 7 (a). With increasing laser power, peak intensities of the carbon C1s peaks decrease and oxygen O1s peaks increase. The corresponding atomic percentages with laser power are plotted in Figure 7 (b). Carbon and oxygen contents in LIGC with increasing laser power vary from 78.4% to 63.1% and 15.3% to 24.8%, respectively. The material starts to oxidize as the power gets close to the ablation limit. Nitrogen N1s intensity is minimal (about 1%) in all cases. Figure 7 (c) shows peaks obtained by deconvolution of each C1s spectrum of the XPS results. The different carbon bonds are predominantly C=C (sp^2) at 284.4 eV [55,56], which is further indication of the high quality of the obtained LIGC. The three different laser powers exhibit very similar percentages of C=C (sp^2) bonds. The biggest difference between LIGC fabricated with these different power values is the different morphology and crystallite size.

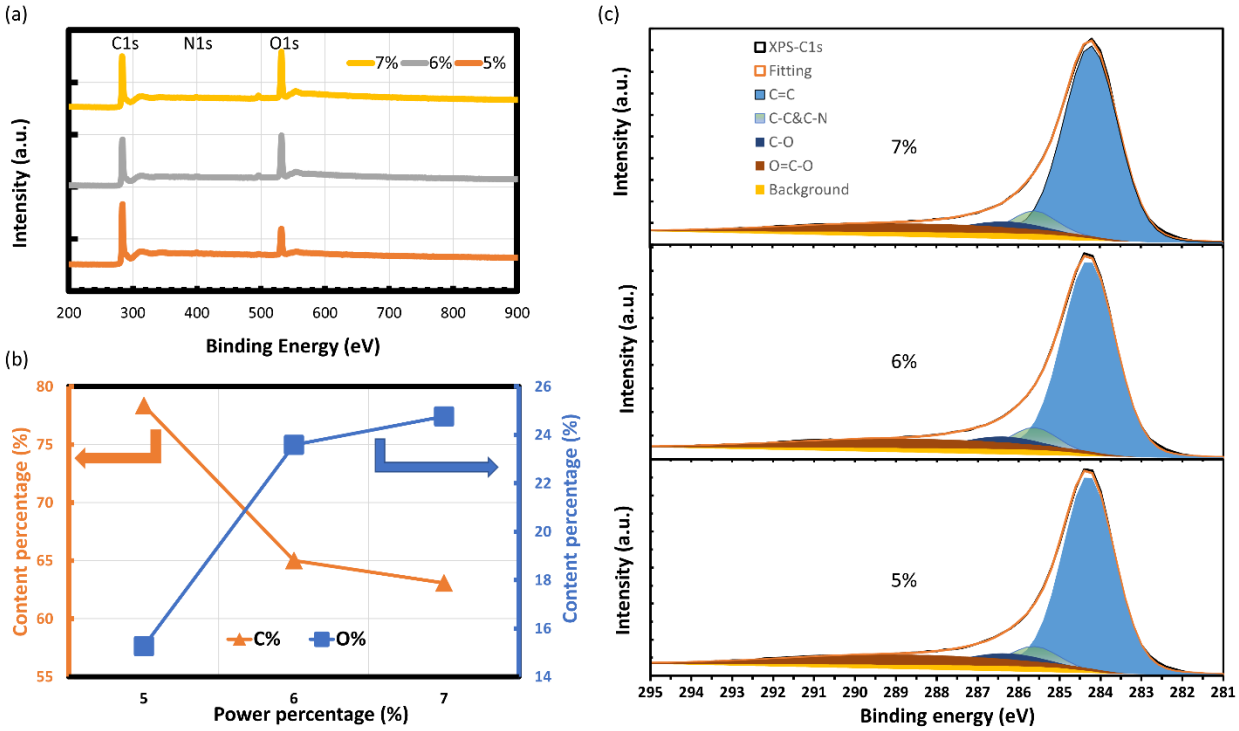

Figure 7. XPS results for LIGC fabricated at 5%, 6%, and 7% laser power (472 DPc, 0.032 m/s). (a) Survey spectra. (b) Carbon (C) and oxygen (O) atomic percentages. (c) Deconvolution of C1s peaks.

3.4. Micro-Supercapacitor Application

To demonstrate an application of the LIGC material, we prepared in-plane micro-supercapacitor devices using LIGC as the electrode material engraved with 7% laser power (highly conductive engraved material). A schematic diagram and image of the prepared micro-supercapacitor are shown in Figure S11. Here, we present its electrochemical properties. This device exhibits high energy and power density compared with other reports.

The prepared device was electrochemically investigated with cyclic voltammetry and galvanostatic charge-discharge measurements and all results are shown in Figure 8. All CV curves (Figure 8 (a)-(b)) at scan rates in the range of 20 mV/s to 10,000 mV/s exhibit capacitive

behavior of the electrochemical double layer at the electrode-electrolyte interface. Formation of the double layer and a high specific capacitance C_A of 0.21 mF/cm^2 at a high scan rate of 10,000 mV/s demonstrates the high performance of the device. All obtained CV capacitances C_A are plotted in Figure 8 (c) for different scan rates. At a low scan rate of 20 mV/s, C_A is 5.1 mF/cm^2. Charge-discharge curves further confirm capacitive behavior. Figure 8 (d) shows charge-discharge curves at various current densities ranging from 0.13 mA/cm^2 to 1.06 mA/cm^2. The calculated capacitances C_A at various current densities are plotted in Figure 8 (e). The micro-supercapacitor can deliver a specific capacitance of 4.8 mF/cm^2 at 0.13 mA/cm^2 and still maintains C_A of 0.46 mF/cm^2 at higher current density of 2.66 mA/cm^2.

The performance of different in-plane micro-supercapacitors can be compared in terms of specific areal energy and power density. The micro-supercapacitor demonstrated here was compared with other micro-supercapacitors prepared by laser engraving of interdigitated electrodes on a PI polymer substrate and using a similar gel electrolyte [21,57–59]. The Ragone plot in Figure 8 (f) shows that it offers high energy and power density.

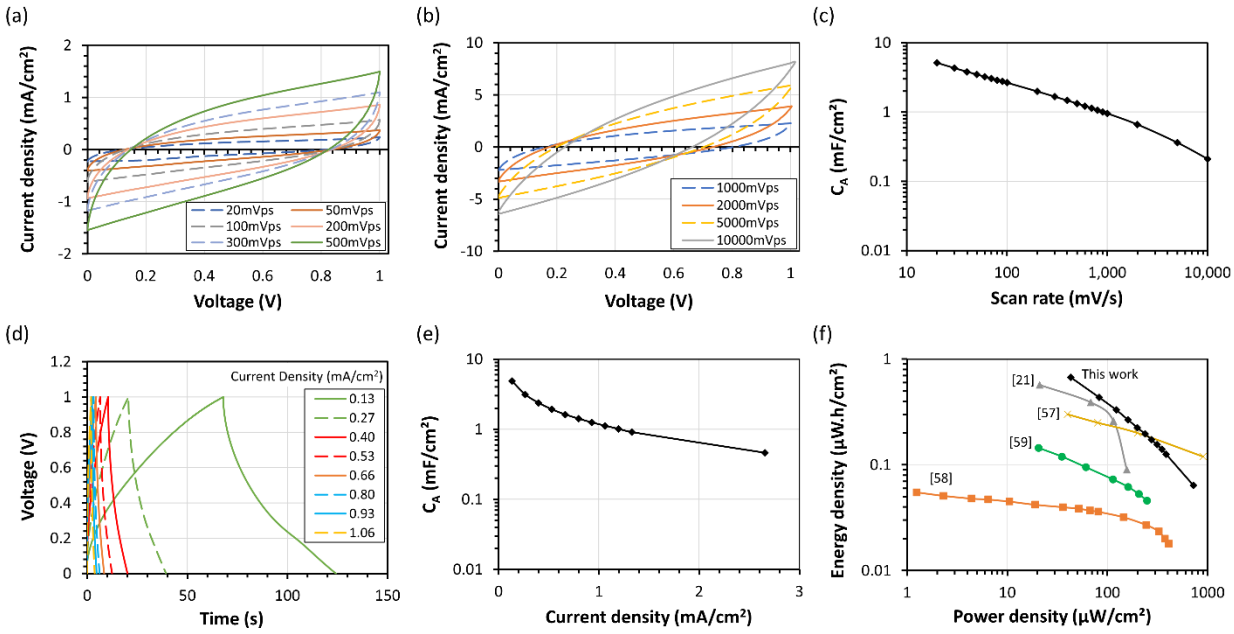

Figure 8. (a) and (b) cyclic voltammetry curves of micro-supercapacitor at scan rates from 20 to 10,000 mV/s. (c) Specific areal capacitance at different scan rates calculated from CV curves. (d) Charge-discharge curves of micro-supercapacitor at different discharge current densities in the range of 0.13 to 1.06 mA/cm^2. (e) Specific areal capacity at different current densities calculated from galvanostatic charge-discharge. (f) Ragone plot of the device in comparison with other results.

4. Conclusion

In this article, the lowest sheet resistance of 6.14±0.11 Ω/□ for LIGC on flexible PI to date is reported. This was achieved by optimizing the following laser conditions: power, scan speed and DPc resolution. DPc plays a vital role because it controls the overlap between adjacent laser pulses. Squares with larger DPc have smaller laser pulse energy but larger energy per unit area. This means the total laser energy delivered to the substrate is larger and more evenly distributed over the surface. Similarly, lines that are only one pulse wide exhibit higher resistance than wider lines because pulses only overlap along the length of the line and not in the transverse direction. More uniform graphitic carbon of high quality can be achieved with more pulse overlap. It was found that to minimize sheet resistance, total energy needs to be maximized

without reaching very high temperatures that cause ablation. This can be achieved by reducing laser scan speed. Thermal modeling shows that lower scan speed allows more time for the material to cool between laser pulses giving a more uniform, less extreme time-temperature profile. Modeling also shows that larger DPc results in a more even spatial temperature distribution. This was further confirmed by SEM, XRD, TEM, scanned Raman spectroscopy, and XPS. Samples with larger DPc exhibit higher-quality and more uniform graphitic carbon. Non-uniformities in the graphitic carbon are periodically spaced corresponding to the spacing of laser pulses. A large crystallite size of about 60 nm was observed. The general strategies developed here can be used to rapidly optimize sheet resistance for any new process development as well as to further push the boundaries of lowest sheet resistance. Moreover, we present a micro-supercapacitor using the low sheet resistance LIGC material exhibiting good electrochemical performance.

Acknowledgements

We acknowledge the support of the Natural Sciences and Engineering Research Council of Canada (NSERC), funding reference number RGPIN-2018-05857. Suresh Nambi was funded by a Mitacs Globalink Research Internship. Samples were laser engraved at the Lassonde School of Engineering Sandbox, York University. SEM images were obtained at the Advanced Light and Electron Microscopy Facility at York University. Raman spectra were measured at the Analytical Laboratory for Environmental Science Research and Training at the University of Toronto. XRD spectra were measured at the Department of Earth Sciences, University of Toronto. TEM images were obtained at the Microscopy Imaging Laboratory at the University of Toronto. XPS spectra were measured at the Ontario Centre for the Characterization of Advanced Materials (OCCAM) at the University of Toronto.

References

[1] H. Kim, J.-H. Ahn, Graphene for flexible and wearable device applications, Carbon. 120 (2017) 244–257. https://doi.org/10.1016/j.carbon.2017.05.041.

[2] T. Das, B.K. Sharma, A.K. Katiyar, J.-H. Ahn, Graphene-based flexible and wearable electronics, J. Semicond. 39 (2018) 011007. https://doi.org/10.1088/1674-4926/39/1/011007.

[3] R. Ye, D.K. James, J.M. Tour, Laser-Induced Graphene: From Discovery to Translation, Adv. Mater. 31 (2019) 1803621. https://doi.org/10.1002/adma.201803621.

[4] N. Kurra, Q. Jiang, P. Nayak, H.N. Alshareef, Laser-derived graphene: A three-dimensional printed graphene electrode and its emerging applications, Nano Today. 24 (2019) 81–102. https://doi.org/10.1016/j.nantod.2018.12.003.

[5] R. You, Y. Liu, Y. Hao, D. Han, Y. Zhang, Z. You, Laser Fabrication of Graphene-Based Flexible Electronics, Adv. Mater. 32 (2020) 1901981. https://doi.org/10.1002/adma.201901981.

[6] A. Zurutuza, C. Marinelli, Challenges and opportunities in graphene commercialization, Nat. Nanotechnol. 9 (2014) 730–734. https://doi.org/10.1038/nnano.2014.225.

[7] W. Xu, T.-W. Lee, Recent progress in fabrication techniques of graphene nanoribbons, Mater Horiz. 3 (2016) 186–207. https://doi.org/10.1039/C5MH00288E.

[8] E. Jabari, F. Ahmed, F. Liravi, E.B. Secor, L. Lin, E. Toyserkani, 2D printing of graphene: a review, 2D Mater. 6 (2019) 042004. https://doi.org/10.1088/2053-1583/ab29b2.

[9] R. Srinivasan, R.R. Hall, W.D. Wilson, W.D. Loehle, D.C. Allbee, Formation of a Porous, Patternable, Electrically Conducting Carbon Network by the Ultraviolet Laser Irradiation of the Polyimide PMDA-ODA (Kapton), Chem. Mater. 6 (1994) 888–889. https://doi.org/10.1021/cm00043a005.

[10] R. Srinivasan, R.R. Hall, W.D. Wilson, W.D. Loehle, D.C. Allbee, Ultraviolet laser irradiation of the polyimide, PMDA-ODA (Kapton^{TM}), to yield a patternable, porous, electrically conducting carbon network, Synth. Met. 66 (1994) 301–307. https://doi.org/10.1016/0379-6779(94)90082-5.

[11] J. Lin, Z. Peng, Y. Liu, F. Ruiz-Zepeda, R. Ye, E.L.G. Samuel, M.J. Yacaman, B.I. Yakobson, J.M. Tour, Laser-induced porous graphene films from commercial polymers, Nat. Commun. 5 (2014) 5714. https://doi.org/10.1038/ncomms6714.

[12] R. Ye, D.K. James, J.M. Tour, Laser-Induced Graphene, Acc. Chem. Res. 51 (2018) 1609–1620. https://doi.org/10.1021/acs.accounts.8b00084.

[13] Y. Zhu, H. Cai, H. Ding, N. Pan, X. Wang, Fabrication of low-cost and highly sensitive graphene-based pressure sensors by direct laser scribing polydimethylsiloxane, ACS Appl. Mater. Interfaces. 11 (2019) 6195–6200.

[14] R. Trusovas, K. Ratautas, G. Račiukaitis, G. Niaura, Graphene layer formation in pinewood by nanosecond and picosecond laser irradiation, Appl. Surf. Sci. 471 (2019) 154–161.

[15] T.D. Le, S. Park, J. An, P.S. Lee, Y. Kim, Ultrafast Laser Pulses Enable One-Step Graphene Patterning on Woods and Leaves for Green Electronics, Adv. Funct. Mater. 29 (2019) 1902771.

[16] R. Ye, Y. Chyan, J. Zhang, Y. Li, X. Han, C. Kittrell, J.M. Tour, Laser-induced graphene formation on wood, Adv. Mater. 29 (2017) 1702211.

[17] Y. Chyan, R. Ye, Y. Li, S.P. Singh, C.J. Arnusch, J.M. Tour, Laser-induced graphene by multiple lasing: toward electronics on cloth, paper, and food, ACS Nano. 12 (2018) 2176–2183.
[18] W. Zhang, Y. Lei, F. Ming, Q. Jiang, P.M. Costa, H.N. Alshareef, Lignin Laser Lithography: A Direct-Write Method for Fabricating 3D Graphene Electrodes for Microsupercapacitors, Adv. Energy Mater. 8 (2018) 1801840.
[19] Z. Peng, J. Lin, R. Ye, E.L.G. Samuel, J.M. Tour, Flexible and Stackable Laser-Induced Graphene Supercapacitors, ACS Appl. Mater. Interfaces. 7 (2015) 3414–3419. https://doi.org/10.1021/am509065d.
[20] L. Li, J. Zhang, Z. Peng, Y. Li, C. Gao, Y. Ji, R. Ye, N.D. Kim, Q. Zhong, Y. Yang, H. Fei, G. Ruan, J.M. Tour, High-Performance Pseudocapacitive Microsupercapacitors from Laser-Induced Graphene, Adv. Mater. 28 (2016) 838–845. https://doi.org/10.1002/adma.201503333.
[21] F. Clerici, M. Fontana, S. Bianco, M. Serrapede, F. Perrucci, S. Ferrero, E. Tresso, A. Lamberti, In situ MoS2 Decoration of Laser-Induced Graphene as Flexible Supercapacitor Electrodes, ACS Appl. Mater. Interfaces. 8 (2016) 10459–10465. https://doi.org/10.1021/acsami.6b00808.
[22] A. Lamberti, F. Perrucci, M. Caprioli, M. Serrapede, M. Fontana, S. Bianco, S. Ferrero, E. Tresso, New insights on laser-induced graphene electrodes for flexible supercapacitors: tunable morphology and physical properties, Nanotechnology. 28 (2017) 174002. https://doi.org/10.1088/1361-6528/aa6615.
[23] L.X. Duy, Z. Peng, Y. Li, J. Zhang, Y. Ji, J.M. Tour, Laser-induced graphene fibers, Carbon. 126 (2018) 472–479.
[24] X. Li, W. Cai, K.S. Teh, M. Qi, X. Zang, X. Ding, Y. Cui, Y. Xie, Y. Wu, H. Ma, Z. Zhou, Q.-A. Huang, J. Ye, L. Lin, High-Voltage Flexible Microsupercapacitors Based on Laser-Induced Graphene, ACS Appl. Mater. Interfaces. 10 (2018) 26357–26364. https://doi.org/10.1021/acsami.8b10301.
[25] I. Karakurt, J. Elwood, X. Li, L. Beker, E. Sweet, W. Cai, L. Lin, Membraneless microfluidic redox battery for wearable electronics applications, in: 2017 19th Int. Conf. Solid-State Sens. Actuators Microsyst. TRANSDUCERS, IEEE, Kaohsiung, Taiwan, 2017: pp. 1820–1823. https://doi.org/10.1109/TRANSDUCERS.2017.7994423.
[26] M. Ren, J. Zhang, J.M. Tour, Laser-induced graphene synthesis of Co3O4 in graphene for oxygen electrocatalysis and metal-air batteries, Carbon. 139 (2018) 880–887. https://doi.org/10.1016/j.carbon.2018.07.051.
[27] D. Vanegas, L. Patiño, C. Mendez, D. Oliveira, A. Torres, C. Gomes, E. McLamore, Laser Scribed Graphene Biosensor for Detection of Biogenic Amines in Food Samples Using Locally Sourced Materials, Biosensors. 8 (2018) 42. https://doi.org/10.3390/bios8020042.
[28] A.R. Cardoso, A.C. Marques, L. Santos, A.F. Carvalho, F.M. Costa, R. Martins, M.G.F. Sales, E. Fortunato, Molecularly-imprinted chloramphenicol sensor with laser-induced graphene electrodes, Biosens. Bioelectron. 124–125 (2019) 167–175. https://doi.org/10.1016/j.bios.2018.10.015.
[29] E.R. Mamleyev, S. Heissler, A. Nefedov, P.G. Weidler, N. Nordin, V.V. Kudryashov, K. Länge, N. MacKinnon, S. Sharma, Laser-induced hierarchical carbon patterns on polyimide substrates for flexible urea sensors, Npj Flex. Electron. 3 (2019). https://doi.org/10.1038/s41528-018-0047-8.

[30] A.C. Marques, A.R. Cardoso, R. Martins, M.G.F. Sales, E. Fortunato, Laser-Induced Graphene-Based Platforms for Dual Biorecognition of Molecules, ACS Appl. Nano Mater. 3 (2020) 2795–2803. https://doi.org/10.1021/acsanm.0c00117.
[31] R. Rahimi, M. Ochoa, W. Yu, B. Ziaie, Highly Stretchable and Sensitive Unidirectional Strain Sensor via Laser Carbonization, ACS Appl. Mater. Interfaces. 7 (2015) 4463–4470. https://doi.org/10.1021/am509087u.
[32] X. Duan, Y. Yao, M. Niu, J. Luo, R. Wang, T. Liu, Direct Laser Writing of Functional Strain Sensors in Polyimide Tubes, ACS Appl. Polym. Mater. 1 (2019) 2914–2923. https://doi.org/10.1021/acsapm.9b00622.
[33] W. Liu, Y. Huang, Y. Peng, M. Walczak, D. Wang, Q. Chen, Z. Liu, L. Li, Stable Wearable Strain Sensors on Textiles by Direct Laser Writing of Graphene, ACS Appl. Nano Mater. 3 (2020) 283–293. https://doi.org/10.1021/acsanm.9b01937.
[34] Y. Ling, W. Pang, X. Li, S. Goswami, Z. Xu, D. Stroman, Y. Liu, Q. Fei, Y. Xu, G. Zhao, B. Sun, J. Xie, G. Huang, Y. Zhang, Z. Yan, Laser-Induced Graphene for Electrothermally Controlled, Mechanically Guided, 3D Assembly and Human-Soft Actuators Interaction, Adv. Mater. (2020) 1908475. https://doi.org/10.1002/adma.201908475.
[35] A. Samouco, A.C. Marques, A. Pimentel, R. Martins, E. Fortunato, Laser-induced electrodes towards low-cost flexible UV ZnO sensors, Flex. Print. Electron. 3 (2018) 044002. https://doi.org/10.1088/2058-8585/aaed77.
[36] M.R. Bobinger, F.J. Romero, A. Salinas-Castillo, M. Becherer, P. Lugli, D.P. Morales, N. Rodríguez, A. Rivadeneyra, Flexible and robust laser-induced graphene heaters photothermally scribed on bare polyimide substrates, Carbon. 144 (2019) 116–126.
[37] M.A. Khan, I.R. Hristovski, G. Marinaro, J. Kosel, Magnetic Composite Hydrodynamic Pump With Laser-Induced Graphene Electrodes, IEEE Trans. Magn. 53 (2017) 1–4. https://doi.org/10.1109/TMAG.2017.2707598.
[38] E.R. Mamleyev, N. Nordin, S. Heissler, K. Lange, N. MacKinnon, S. Sharma, Flexible Carbon-based Urea Sensor by Laser Induced Carbonisation of Polyimide, in: 2018 Int. Flex. Electron. Technol. Conf. IFETC, IEEE, Ottawa, ON, 2018: pp. 1–6. https://doi.org/10.1109/IFETC.2018.8583942.
[39] X. Ruan, R. Wang, J. Luo, Y. Yao, T. Liu, Experimental and modeling study of CO2 laser writing induced polyimide carbonization process, Mater. Des. 160 (2018) 1168–1177.
[40] S. Venkatachalam, M. Depriester, A.H. Sahraoui, B. Capoen, M.R. Ammar, D. Hourlier, Thermal conductivity of Kapton-derived carbon, Carbon. 114 (2017) 134–140. https://doi.org/10.1016/j.carbon.2016.11.072.
[41] S. Küper, J. Brannon, K. Brannon, Threshold behavior in polyimide photoablation: Single-shot rate measurements and surface-temperature modeling, Appl. Phys. Solids Surf. 56 (1993) 43–50. https://doi.org/10.1007/BF00351902.
[42] H. Hatori, Y. Yamada, M. Shiraishi, M. Yoshihara, T. Kimura, The mechanism of polyimide pyrolysis in the early stage, Carbon. 34 (1996) 201–208. https://doi.org/10.1016/0008-6223(96)00189-3.
[43] B.E. Warren, X-Ray Diffraction in Random Layer Lattices, Phys. Rev. 59 (1941) 693–698. https://doi.org/10.1103/PhysRev.59.693.
[44] W. Zhang, Y. Lei, Q. Jiang, F. Ming, P.M. Costa, H.N. Alshareef, 3D Laser Scribed Graphene Derived from Carbon Nanospheres: An Ultrahigh-Power Electrode for Supercapacitors, Small Methods. 3 (2019) 1900005.

[45] A.C. Ferrari, J. Meyer, V. Scardaci, C. Casiraghi, M. Lazzeri, F. Mauri, S. Piscanec, D. Jiang, K. Novoselov, S. Roth, Raman spectrum of graphene and graphene layers, Phys. Rev. Lett. 97 (2006) 187401.
[46] A.C. Ferrari, Raman spectroscopy of graphene and graphite: Disorder, electron–phonon coupling, doping and nonadiabatic effects, Solid State Commun. 143 (2007) 47–57. https://doi.org/10.1016/j.ssc.2007.03.052.
[47] M.A. Pimenta, G. Dresselhaus, M.S. Dresselhaus, L.G. Cançado, A. Jorio, R. Saito, Studying disorder in graphite-based systems by Raman spectroscopy, Phys Chem Chem Phys. 9 (2007) 1276–1290. https://doi.org/10.1039/B613962K.
[48] L.G. Cançado, K. Takai, T. Enoki, M. Endo, Y.A. Kim, H. Mizusaki, N.L. Speziali, A. Jorio, M.A. Pimenta, Measuring the degree of stacking order in graphite by Raman spectroscopy, Carbon. 46 (2008) 272–275. https://doi.org/10.1016/j.carbon.2007.11.015.
[49] I. Pócsik, M. Hundhausen, M. Koós, L. Ley, Origin of the D peak in the Raman spectrum of microcrystalline graphite, J. Non-Cryst. Solids. 227 (1998) 1083–1086.
[50] Y. Zhu, H. Cai, H. Ding, N. Pan, X. Wang, Fabrication of low-cost and highly sensitive graphene-based pressure sensors by direct laser scribing polydimethylsiloxane, ACS Appl. Mater. Interfaces. 11 (2019) 6195–6200.
[51] Z. Wang, G. Wang, W. Liu, B. Hu, J. Liu, Y. Zhang, Patterned laser-induced graphene for terahertz wave modulation, J. Opt. Soc. Am. B. 37 (2020) 546–551. https://doi.org/10.1364/JOSAB.383324.
[52] F. Wang, W. Duan, K. Wang, X. Dong, M. Gao, Z. Zhai, X. Mei, J. Lv, W. Wang, C. Zhu, Graphitized hierarchically porous carbon nanosheets derived from bakelite induced by high-repetition picosecond laser, Appl. Surf. Sci. 450 (2018) 155–163. https://doi.org/10.1016/j.apsusc.2018.04.130.
[53] Y. Lu, H. Lyu, A.G. Richardson, T.H. Lucas, D. Kuzum, Flexible neural electrode array based-on porous graphene for cortical microstimulation and sensing, Sci. Rep. 6 (2016) 33526.
[54] F. Wang, X. Mei, K. Wang, X. Dong, M. Gao, Z. Zhai, J. Lv, C. Zhu, W. Duan, W. Wang, Rapid and low-cost laser synthesis of hierarchically porous graphene materials as high-performance electrodes for supercapacitors, J. Mater. Sci. 54 (2019) 5658–5670. https://doi.org/10.1007/s10853-018-03247-0.
[55] H. Wu, W. Zhang, S. Kandambeth, O. Shekhah, M. Eddaoudi, H.N. Alshareef, Conductive Metal–Organic Frameworks Selectively Grown on Laser-Scribed Graphene for Electrochemical Microsupercapacitors, Adv. Energy Mater. 9 (2019) 1900482.
[56] Z. Wan, M. Umer, M. Lobino, D. Thiel, N.-T. Nguyen, A. Trinchi, M.J. Shiddiky, Y. Gao, Q. Li, Laser induced self-N-doped porous graphene as an electrochemical biosensor for femtomolar miRNA detection, Carbon. (2020).
[57] W. Zhang, Q. Jiang, Y. Lei, H.N. Alshareef, Wettability-Driven Assembly of Electrochemical Microsupercapacitors, ACS Appl. Mater. Interfaces. 11 (2019) 20905–20914. https://doi.org/10.1021/acsami.9b05635.
[58] X. Shi, F. Zhou, J. Peng, R. Wu, Z.-S. Wu, X. Bao, One-Step Scalable Fabrication of Graphene-Integrated Micro-Supercapacitors with Remarkable Flexibility and Exceptional Performance Uniformity, Adv. Funct. Mater. 29 (2019) 1902860. https://doi.org/10.1002/adfm.201902860.
[59] Y. Li, D.X. Luong, J. Zhang, Y.R. Tarkunde, C. Kittrell, F. Sargunaraj, Y. Ji, C.J. Arnusch, J.M. Tour, Laser-Induced Graphene in Controlled Atmospheres: From

792 Superhydrophilic to Superhydrophobic Surfaces, Adv. Mater. 29 (2017) 1700496.
793 https://doi.org/10.1002/adma.201700496.
794

795